The Cryosphere Discuss., doi:10.5194/tc-2017-41, 2017
Manuscript under review for journal The Cryosphere
Discussion started: 7 April 2017

Detecting high spatial variability of ice-shelf basal mass balance (Roi Baudouin ice shelf, Antarctica)

Sophie Berger[1], Reinhard Drews[2], Veit Helm[3], Sainan Sun[1], and Frank Pattyn[1]
[1]Laboratoire de glaciologie, Université libre de Bruxelles, Brussels, Belgium
[2]Bavarian Academy of Sciences and Humanities, Munich, Germany
[3]Alfred Wegener Institute, Bremerhaven, Germany
Correspondence to: S. Berger (sberger@ulb.ac.be)

Abstract.

Ice shelves control the dynamic mass loss of ice sheets through buttressing and their integrity depends on the spatial variability of their basal mass balance (BMB), i.e., the difference between refreezing and melting. Here, we present a novel technique – based on satellite observations – to capture the small-scale variability in the BMB of ice-shelves. As a case study we apply the methodology to the Roi Baudouin Ice Shelf, Dronning Maud Land, East Antarctica and derive its yearly-averaged BMB at 10 m horizontal gridding. We use mass conservation within a Lagrangian framework based on high-resolution surface velocities, atmospheric-model surface mass balance and hydrostatic ice-thickness fields (derived from TanDEM-X surface elevation). Spatial derivatives are implemented using the total-variation differentiation, which avoids spatial averaging hence loss of spatial resolution. Our BMB field exhibits high detail and ranges from -14.8 to 8.6 m a^{-1} ice equivalent. Highest melt rates are found close to the grounding line where the basal ice-shelf slope is the steepest. The BMB field agrees well with on-site measurements from phase-sensitive radar, although unresolved spatial variations in firn density determined from profiling radar occur. We show that the surface expression of an englacial lake (0.7×1.3 km^2 wide and 30 m deep) lowers by 0.5 to 1.4 m a^{-1}, which we tentatively attribute to a transient adaptation to hydrostatic equilibrium. We find evidence for elevated melting beneath ice-shelf channels (with melting being concentrated on the channel's flanks). However, farther downstream from the grounding line, the majority of ice-shelf channels advect passively toward the ice-shelf front. Although the absolute, satellite-based BMB values remain uncertain, we have high confidence in the spatial variability on sub-kilometre scales. This study highlights expected challenges for a full coupling between ice and ocean models.

1 Introduction

Approximately 74% of the Antarctic ice sheet is surrounded by floating ice shelves (Bindschadler et al., 2011a) providing the interface for interactions between ice and ocean. Marine ice sheets – characterized by a bed elevation below sea level and sloping down towards the interior – can be destabilised leading to a Marine Ice Sheet Instability (Mercer, 1978; Schoof, 2007; Tsai et al., 2015). However, ice shelves that are laterally constrained through embayments (or locally regrounded from below), mitigate the Marine Ice Sheet Instability (Gudmundsson et al., 2012), thus regulating the ice flux from the inland ice sheet through buttressing. Over the last decade, major advances in our understanding of the processes at this ice-ocean interface emerged, both theoretically (e.g. Pattyn et al., 2013; Favier et al., 2012, 2014; Ritz et al., 2015) as well as from observations (e.g. Rignot et al., 2014; Wouters et al., 2015). It is now established that ice-shelf integrity plays an important part in explaining sea-level variations in the past (Golledge et al., 2014; DeConto and Pollard, 2016), enabling improved projections of future sea-level rise (Golledge et al., 2015; Ritz et al., 2015).

While oceanic processes play a dominant role in ice-shelf basal mass balance, ice-shelf integrity can be further compromised by atmospheric driven surface melt-ponding (Lenaerts et al., 2017) and hydrofracturing (Banwell et al., 2013; Scambos et al., 2004; Hulbe et al., 2004). From the ocean side, ice shelves may thin or thicken (Paolo et al., 2015) due to changes in basal mass balance (BMB), i.e. the difference between refreezing and melting. Point measurements with phase-sensitive radars (Marsh et al., 2016; Nicholls et al., 2015), observations from underwater vehicles (Dutrieux et al., 2014) and analysis from high-resolution satellites (Dutrieux et al., 2013) have shown that the BMB varies spatially on sub-kilometre scales. Ice-shelf channels are one expression of localised melting (Stanton et al., 2013; Marsh et al., 2016) which forms curvilinear tracts in ice shelves where ice is more than 50 % thinner than its surrounding (Drews, 2015). However, the impact of ice-shelf channels on ice-shelf integrity is yet unclear because, on the one hand, excessive basal melting beneath ice-shelf channels may prevent ice-shelf-wide thinning (Gladish et al., 2012; Millgate et al., 2013) but, on the other hand, increased crevassing due to channel carving may structurally weaken the ice shelf (Vaughan et al., 2012).

Here we attempt to derive the BMB of the Roi Baudouin Ice Shelf (RBIS), Dronning Maud Land, East Antarctica, at 10 m gridding, based on mass conservation in a Lagrangian framework. The RBIS (Fig.1) is constrained by an ice promontory to the West and by Derwael Ice Rise in the East, blocking the tributary flow from Western Ragnhild Glacier, one of the largest outlet glaciers in Dronning Maud Land (Callens et al., 2014). Analysis on Derwael Ice Rise (Drews et al., 2015; Callens et al., 2016) and the larger catchment area (Favier et al., 2016) suggest that the RBIS is a relatively stable sheet-shelf system on millennial time scales. The RBIS contains a number of ice-shelf channels (Drews, 2015, and arrows in Fig. 2e), many of which start at the grounding line and extend over 230 km all the way to the ice-shelf front.

In the following, we outline our approach of deriving the BMB, with a special focus on attaining high spatial resolution results. Resolving BMB is challenging, because it is computed as the residual of large numbers and it relies on spatial derivatives, which amplify noise in the input data. The latter can be accounted for with spatial averaging (e.g. Neckel et al., 2012; Moholdt et al., 2014), which, however, may smear out the processes acting on sub-kilometre scales. Here, we use spatially well-resolved input data combined with total-variation regularization of the velocity gradients. This avoids spatial averaging, but still accounts for the noise in the input data. As a result, our BMB field shows high detail over different spatial scales that are validated with phase-sensitive and ground-penetrating radar observational evidence, as well as kinematic global navigation satellite system (GNSS) profiling.

The Cryosphere Discuss., doi:10.5194/tc-2017-41, 2017
Manuscript under review for journal The Cryosphere
Discussion started: 7 April 2017

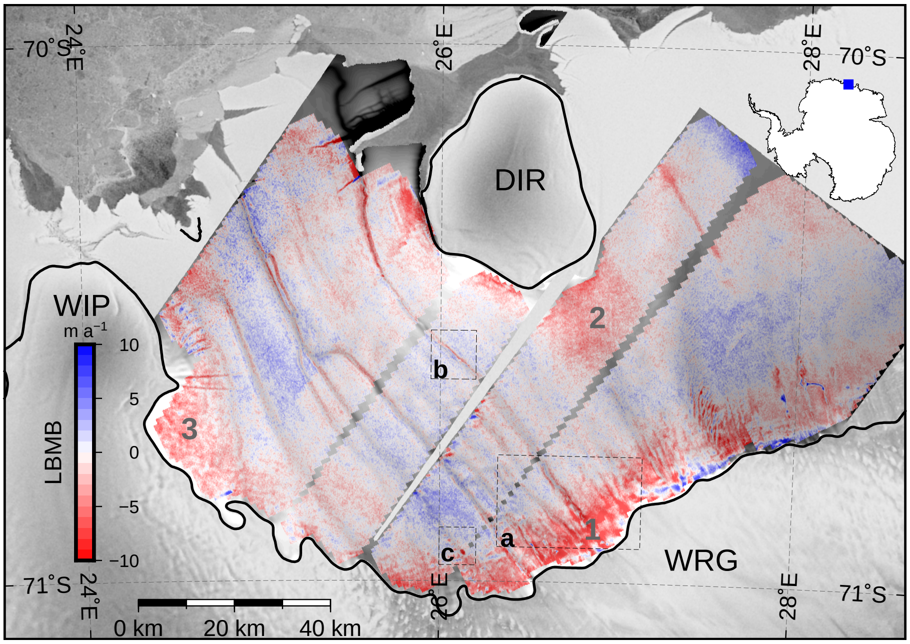

Figure 1. Lagrangian Basal Mass Balance (LBMB) of the Roi Baudouin Ice Shelf. Red and blue colours indicate basal melting and refreezing, respectively. Insets (a), (b) and (c) locate the close-ups presented in figures 4, 5 and 7. Labels 1-3 pinpoint areas discussed in the text. Acronyms stand for DIR: Derwael Ice Rise, WIP : Western Ice Promontory and WRG: West Ragnhild Glacier. The LBMB overlays the 2014 TanDEM-X DEM in slight transparency. The background is from the Radarsat mosaic (Jezek and RAMP-Product-Team, 2002) and the black line delineates the grounding line (Depoorter et al., 2013).

2 Method

2.1 Basal mass balance from mass conservation

We derived the basal mass balance ($\dot{M}_b$) from mass conservation, i.e.,

$$\begin{aligned}\dot{M}_b &= \frac{\partial H}{\partial t} + \nabla\cdot(H\boldsymbol{u}) - \dot{M}_s\\ &= \frac{\partial H}{\partial t} + (\boldsymbol{u}\cdot\nabla H + H\nabla\cdot\boldsymbol{u}) - \dot{M}_s\\ &= \frac{\mathrm{D}H}{\mathrm{D}t} + H\,(\nabla\cdot\boldsymbol{u}) - \dot{M}_s\end{aligned} \tag{1}$$

where $\dot{M}_s$ is the surface mass balance (SMB, positive values for mass gain), H is the ice thickness and $\boldsymbol{u}$ the vertically-integrated horizontal ice velocity. $\dot{M}_b$, $\dot{M}_s$ and H are given in ice-equivalent units. In principle eq. (1) does not depend on the reference frame and can be calculated in both a fixed coordinate system (i.e. Euler coordinates) or with a moving coordinate system that follows the ice flow (i.e. Lagrange coordinates). In practice, however, both approaches differ greatly: an Eulerian coordinate system requires only one thickness field in time and typically accounts for the thickness change $\partial H/\partial t$ explicitly (Depoorter et al., 2013; Rignot et al., 2013) or assumes a steady-state (Rignot and Steffen, 2008; Neckel et al., 2012). The Lagrangian approach, however, requires two thickness fields covering different time periods from which the Lagrangian thickness change is calculated implicitly ($\mathrm{D}H/\mathrm{D}t$). As shown below, the key difference between both approaches is how the advection of thickness gradients ($\boldsymbol{u}\cdot\nabla H$) is accounted for. In areas where advection is significant (e.g. near ice-shelf channels), this can only be adequately done in a Lagrangian framework. We refer to previous publications (Dutrieux et al., 2013; Moholdt et al., 2014) that further explain differences between Eulerian and Lagrangian approaches.

We describe surface velocities in section 2.2, SMB in section 2.3 and the derivation of hydrostatic ice thickness in section 2.4. As a novelty compared to previous studies, we base our hydrostatic thickness field on high-resolution digital elevation models (DEMs) derived from TanDEM-X images of 2013 and 2014, clearly resolving ice-shelf channels. Section 2.5 explains the implementation of spatial velocity gradients ($\nabla\cdot\boldsymbol{u}$ in eq. (1)), which is non-trivial when derivatives are taken over short distances with noisy input data. We calculate the Lagrangian thickness change $\mathrm{D}H/\mathrm{D}t$ by cross-correlating the TanDEM-X DEMs (using 5×5 km^2 patches and a normalized cross-correlation threshold of 0.8). We also investigate an alternative approach of using the observed surface velocities to shift the thickness field (Moholdt et al., 2014, and section 4).

We compare the derived Lagrangian Basal Mass Balance (LBMB) with field measurements of phase-sensitive radar and GNSS profiling (section 2.6). Although this is not a direct validation, as the field data cover a different period, the comparison is insightful to understand the spatial variability in our LBMB field. The derived LBMB is only valid in freely floating areas, which excludes the grounding zone, but also other small-scale features such as viscous inflow in ice-shelf channels (Humbert et al., 2015; Drews, 2015). Examples where this may be the case are discussed in section 5.

2.2 Surface velocities from satellite radar remote sensing

We use surface velocities that were previously derived by combining interferometric Synthetic Aperture Radar (InSAR) and speckle tracking (Berger et al., 2016). The velocities are gridded to a 125 m posting and based on images from the European Remote Sensing satellites (ERS 1/2) of 1996 and the Advanced Land Observing System Phased Array type L-band Synthetic Aperture Radar (ALOS-PALSAR) of 2010. Comparison with on-site GNSS measurements collected in 2014 yields no evidence for temporal variations in the yearly averaged ice velocities. This dataset covers 75% of our area of interest. The remaining areas are filled in with an Antarctic-wide flow field (Rignot et al., 2011) gridded to a 900 m posting (the 450 m gridded velocities being too noisy in our area of interest). We reduce cutting edges – as high as 60 m a^{-1} in some places – using linear feathering over 4.5 km.

2.3 Surface mass balance from atmospheric modelling

The SMB is based on a high-resolution (5.5 km posting) simulation of the Regional Atmospheric Climate MOdel (RACMO) version 2.3, centred on Dronning Maud Land (25°W and 45°W) and spanning 1979–2015 (Lenaerts et al., 2014, 2017). The SMB field correctly reproduces asymmetries across Derwael Ice Rise originating from orographic uplift and also predicts a

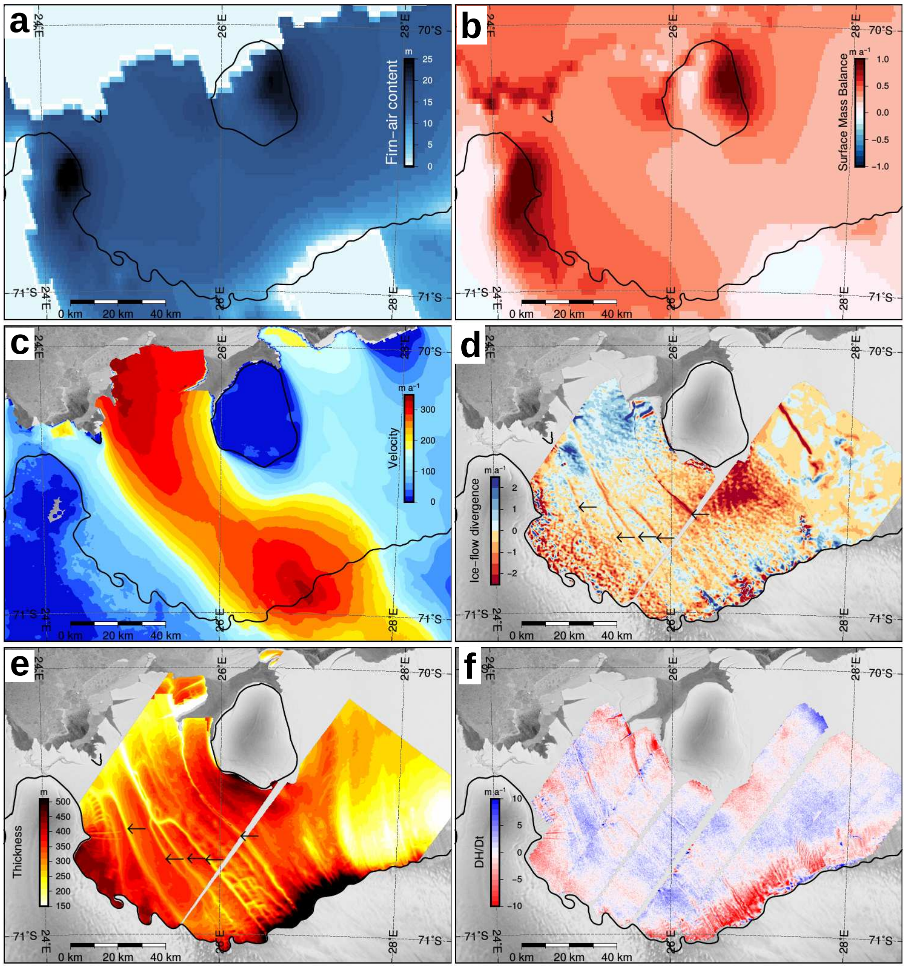

Figure 2. (a, c, e) Variables entering Eqs. (1) and (2) and (b, d , f) terms needed to calculate the LBMB in Eq. (1). (a) Firn-air content (H_a); (b) surface mass balance ($\dot{M}_s$); (c) surface velocities ($\boldsymbol{u}$); (d) ice-flow divergence ($H\,(\nabla\cdot\boldsymbol{u})$); (e) hydrostatic ice thickness of 2014 (H) and (f) Lagrangian thickness change ($\mathrm{D}H/\mathrm{D}t$). Arrows in (d) and (e) locate ice-shelf channels. The background is from the Radarsat mosaic (Jezek and RAMP-Product-Team, 2002) and the black line delineates the grounding line (Depoorter et al., 2013).

corresponding shadowing effect on the Roi Baudouin Ice Shelf. Moreover, the simulation explains observed surface melting near the grounding zone due to a wind-albedo feedback caused by persistent katabatic winds in this area (Lenaerts et al., 2017).

2.4 Hydrostatic Ice Thickness

We calculate the ice thickness by imposing hydrostatic equilibrium on surface freeboard (Bindschadler et al., 2011b; Chuter and Bamber, 2015; Drews, 2015). The DEMs were processed from 43 image pairs of the TanDEM-X mission. The TerraSAR-X and TandDEM-X satellites image the surface simultaneously from different viewing angles, hence allow inferring the topography interferometrically without the need to correct for ice flow. Images from the austral winters of 2013 and 2014 are processed to single-look complex scenes, using SARscape. After coregistration using the CryoSat-2 DEM (Helm et al., 2014), the pairs are differenced in phase. The resulting interferograms are then unwrapped and the phase difference is re-flattened before being geo-referenced in polar stereographic coordinates. The processing provides 43 single DEMs (32 from 2013 and 11 from 2014) gridded to 10 m with an estimated relative vertical accuracy better than 1 m (based on the standard deviation in overlapping areas). DEMs from the same date and satellite path are concatenated together, with a linear taper on overlapping zones. Grounded areas are masked out using the grounding line from Depoorter et al. (2013). DEMs based on SAR interferometry can exhibit a flawed elevation trend due to imprecise information about the satellite orbits or due to parameter estimation during the SAR processing (Drews et al., 2009). In our case, this is evident in the difference fields of the individual DEMs, which exhibit a linear trend aligned with the satellite trajectory. We correct for this by fitting a plane to the difference field that is subtracted from the 2014 DEMs. This adjustment is further discussed in section 4. Additionally, all DEMs are smoothed with a Gaussian filter removing small-scale surface roughness. The standard deviation of the Gaussian filter was set to 7, because it minimizes the mean and standard deviation of the difference between the TanDEM-X DEMs and GNSS profiles collected on-site. The quality of our ice-thickness fields and the resulting BMB rates, strongly depend on the corrections applied here, which is further discussed in section 4.

We apply the hydrostatic equilibrium on freeboard heights (h_{asl}) with densities of $\rho_w = 1027\ kg\ m^{-3}$, $\rho_i = 910\ kg\ m^{-3}$ and $\rho_a = 2\ kg\ m^{-3}$, for seawater, ice and firn air, respectively :

$$H = \frac{\rho_w h_{asl}}{\rho_w - \rho_i} - \frac{H_a(\rho_w - \rho_a)}{\rho_w - \rho_i}. \tag{2}$$

The firn-air content H_a accounts for the variable firn density by subdividing the ice column in air- and ice-equivalent layers. We use simulated values from the firn-densification model 'IMAU-FDM' (Ligtenberg et al., 2011; Lenaerts et al., 2017), which is forced by the SMB and exists on the same spatial grid (5.5 km, section 2.3). For converting ellipsoidal heights to freeboard elevations we employ the EIGEN-6C4 geoid (Förste et al., 2014) and the DTU12MDT mean dynamic topography model (Knudsen and Andersen, 2012). The hydrostatic ice thickness is most sensitive to the firn-air content and the freeboard height, resulting in an estimated uncertainty of at least ± 25 m (Drews, 2015). However, as discussed below, uncertainties can be much higher in areas where firn density is ill-constrained.

2.5 Spatial derivatives with noisy input data

Taking spatial gradients in eq. (1) is not straightforward as naive discretization schemes (e.g. forward, backward or central differences) greatly amplify the signal-to-noise ratio if the input data are noisy. Although this is typically accounted for by smoothing the input data (e.g. Moholdt et al., 2014) and/or by increasing the lateral distances over which the derivative is approximated (e.g. Neckel et al., 2012), it is largely unsuited to resolve small-scale features such as ice-shelf channels. Smoothing the surface velocities with a kernel comparable to the size of ice-shelf channels subdues small-scale anomalies in the flow field (e.g. lateral convergence), which can accompany locally elevated basal melt rates (Drews, 2015). To circumnavigate this problem, we applied the total-variation regularization, which formulates the derivative as an inverse problem, and where the wiggliness of the derivative is controlled through a regularization parameter α (Chartrand, 2011). By exploring α values ranging from 1 to 10^6, the value of 10^5 was retained as the best trade-off between noise reduction and loss of small-scale variability. Fig. 7 compares a regularized derivative with a derivative based on central differences and smoothed input data, which we discuss in section 4. This α value was chosen considering the standard deviation between the observed and regularized velocities (resulting from the integration of the regularized derivatives). $\alpha = 10^5$ results in a standard deviation of 4.5 m/a at the centre of our area of interest, which approximately corresponds to our estimated error in the velocities and suggests that with this alpha the regularization successfully suppresses the noise while keeping the signal. However, some ambiguity about the specific choice of α remains, which is inherent to regularization in general.

2.6 On-site geophysical measurements

During the Austral winter of 2015-2016, a series of geophysical measurements were carried out on the RBIS, such as ground-penetrating radar, GNSS profiling and phase-sensitive radar measurements.

The ground-penetrating radar profile shown in Fig. 6a was acquired with a 20 MHz pulsed radar (Matsuoka et al., 2012). The data were geolocated with kinematic GNSS and migrated using Kirchoff-depth migration with a velocity-depth function that accounts for the low firn-air content in this area. More details about acquisition and processing of the radar data are given in Drews et al. (2015). We use the radar ice thickness to validate the hydrostatic ice thickness (section 4).

The kinematic GNSS profiles were recorded at 1 Hz intervals with geodetic, multi-channel receivers moving at a speed below 12 km h^{-1}. The data were processed differentially, relative to a non-moving base station (Drews et al., 2015). Elevations were de-tided using the circum-Antarctic tide model (CATS2008a_opt) from Padman et al. (2002, 2008). The same data is used to extend the time period of surface elevation change detected by the TanDEM-X mission.

BMB was measured at point locations using a phase-sensitive radar. Processing and acquisition schemes are as outlined previously (Nicholls et al., 2015; Marsh et al., 2016). The radar antennas were positioned at 22 sites. Each site was remeasured after 10 days at exactly the same location at the surface (in a Lagrangian framework). This way, relative thickness changes due to strain thinning and basal melting can be detected within millimetres. Strain thinning is corrected using a linear approximation of the vertical strain rate with depth, based on tracking the relative displacement of internal reflectors. The strain correction of

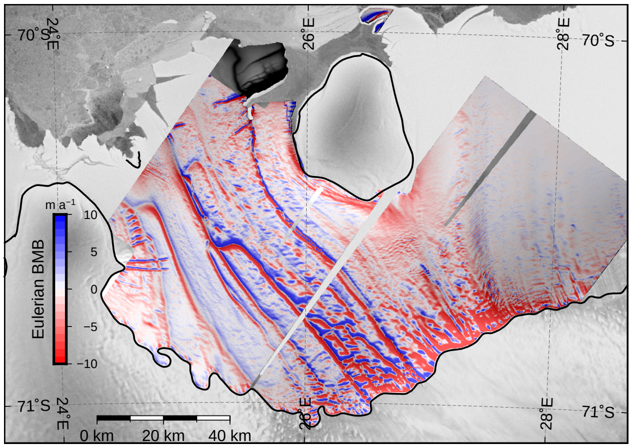

Figure 3. Eulerian Basal Mass Balance in steady state ($\partial H/\partial t = 0$), overlaying the 2014 TanDEM-X DEM in slight transparency. The background is from the Radarsat mosaic (Jezek and RAMP-Product-Team, 2002) and the black line delineates the grounding line (Depoorter et al., 2013).

the BMB rates is small (6.6×10^{-3} m a^{-1} on average), because strain thinning in the 10-day interval is small compared to the inferred basal melt rates, i.e., approximately 1.1 m a^{-1}.

3 Results

3.1 Large-scale pattern of the Basal mass balance

The LBMB rates range from -14.8 to 8.6 m a^{-1} and average -0.8 m a^{-1} (negative values signify melting, positive values refreezing). Fig. 1 shows that most melting occurs just seawards of the grounding zone where the western Ragnhild Glacier feeds into the Roi Baudouin Ice Shelf (label 1). This area corresponds to the thickest and fastest part of the grounding zone (Fig. 2e and c). We also find elevated melting close to the western ice promontory (label 2) and on the stoss side of Derwael Ice Rise (label 3). The uncertainties of the absolute LBMB are typically higher than the LBMB itself, because errors unfavourably propagate in mass budgets (Moholdt et al., 2014). Here, we assess a lower bound of the LBMB errors by using the difference fields of the individual LBMB frames in overlapping areas. These show no systematic patterns and the standard deviation amounts to 2.3 m a^{-1}. Moreover, comparing the (yearly averaged) LBMB values with the 22 on-site, 10-day averaged phase-sensitive radar measurements, reveals differences of 1.1±2.6m a^{-1} in mean and standard deviation, respectively. Qualitatively, the large-scale pattern agrees well with the results from Rignot et al. (2013) who also found the highest melt rates close to the grounding line, both for steady state or transient approximations. To demonstrate the necessity of the Lagrangian approach, we also calculate the BMB in a steady-state Eulerian framework. As shown in Fig. 3, this results in spurious signals in particular close to ice-shelf channels, due to advection of thickness gradients ($\boldsymbol{u} \cdot \nabla H$) that are not adequately accounted for. A high-resolution, transient version of the Eulerian thickness change is difficult, because the thinning/thickening rates ($\partial H/\partial t$) have

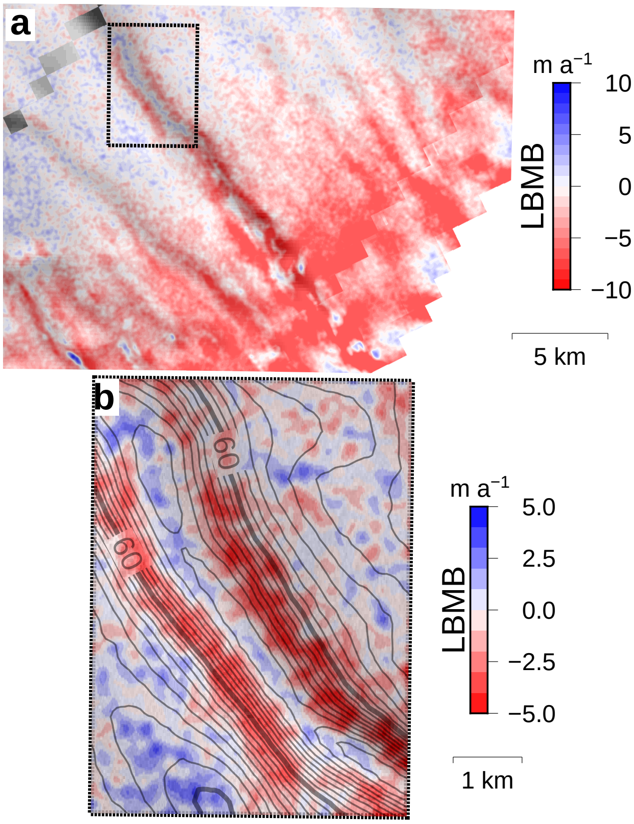

Figure 4. Close-up of the LBMB near the grounding line, where enhanced melting collocates with ice-shelf channels (a) Zoomed-in version of inset a in Fig. 1. (b) Close-up at one channel with 1 m elevation contour lines overlain.

to be prescribed from external datasets, which are typically not well resolved. Using ice-shelf wide, average values (e.g. repeat satellite altimetry) does not account for the advection of ice-shelf channels and other (transient) features in the ice-shelf, hence violating the steady-state assumption.

Figs. 2b,d,f illustrate the terms entering Eq. (1), i.e., SMB, ice-flow divergence and Lagrangian thickness change, whereas Figs. 2a,c,e display the most critical input variables needed to compute those different terms, i.e., firn-air content, ice velocity and hydrostatic thickness. For the RBIS, the Lagrangian thickness change dominates the BMB (as in Shean et al., 2017), while the ice-flow divergence and the SMB are both one order of magnitude lower.

3.2 Small-scale variability

The larger scale BMB pattern (>10 km) is overlain by smaller-scale variability. Ice-shelf channels appear most clearly in the DEMs and the hydrostatic thickness fields (arrows in Fig. 2e). To a lesser extent, they also co-locate with areas of lateral inflow (i.e., negative flow divergence; arrows in Fig. 2d) and Lagrangian thinning (i.e., negative Lagrangian thickness change in Fig. 2f). In the LBMB, ice-shelf channels appear partially as narrow bands of intense melting (e.g. insets a and b in Fig. 1). Fig. 4 shows one example where ice preferentially melts at the flanks of an ice-shelf channel. LBMB rates drop to -5m a^{-1} at both flanks, whereas outside the channel and at the channel's apex, the LBMB is close to zero.

Another example of a small-scale feature is illustrated in Figs. 5 and 6. Here, we observe a 0.7×1.3 km^2 ellipsoidal surface depression which is connected to an ice-shelf channel on its downstream end (Fig 5a). The surface topography also exhibits secondary elongated surface depressions that merge like tributaries into the ellipsoidal depression (marked with arrows in Fig. 5). We surveyed this area in 2016 with kinematic GNSS profiles of ground-penetrating radar and 22 point-measurements of the LBMB with phase-sensitive radar (section 2.6). Lenaerts et al. (2017) identified this feature as one of the 55 englacial lakes on the Roi Baudouin Ice Shelf. They proposed that these lakes are at first supra-glacial and form in the grounding zone due to katabatic wind-albedo feedback. Freezing at the lake surface and subsequent burial by snowfalls form the englacial lakes that are advected farther downstream. In this case, the hypothesized water-ice interface is at approximately 30 m depth and blocks the penetration of radar waves (Fig. 6a). With today's surface velocities, it would require ~50 years for the lake to be advected from the grounding line to its current position. We have no direct evidence for an englacial lake at this location and it is also possible that radar penetration is blocked by some other internal, specular reflector (such as a refrozen surface of a former lake). The specifics of this interface, however, are not important here as we focus exclusively on its surface expression. The englacial lake area appears prominently in our LBMB field with rates down to -12 m a^{-1} (Figs. 6b and 5b). Outside the englacial lake area, the BMB from the phase-sensitive radar (Fig. 6b) agrees well with the LBMB estimate. On the eastern side, we find a near-perfect fit with both methods averaging about -0.5 m a^{-1} with little spatial variability. On the western side – which contains the surface tributaries – larger differences and variability occur. The low LBMB rates in the englacial lake area are caused by persistent surface lowering of 0.5 to 1.4 m a^{-1} because ice-flow divergence is negligible at that location. We extend the time series to 2016 with the GNSS profiles (Fig. 6c) where we find the same localized lowering. This shows that the high-resolution TanDEM-X DEMs reliably pick up surface elevation changes on sub-kilometre scales. Some of the surface tributaries also show surface lowering, but less pronounced than what is seen in the englacial lake area itself. The flanks of the ellipsoidal surface depression are significantly steeper on the eastern compared to the western side. Unlike the englacial lake area, the connected ice-shelf channel located farther downstream appears inactive. Outside the lake area, our assumptions for the LBMB (such as hydrostatic equilibrium) likely hold explaining the comparatively good fit with the phase-sensitive radar measurements. Inside the lake area, the observed surface lowering must not solely be attributed to basal melting, but may also reflect viscous inflow (Humbert et al., 2015) or creeping of the englacial lake through the ice column. Regardless of the specific mechanisms causing the surface lowering, this example highlights that much of the small-scale variability seen in the LBMB field can be used to investigate sub-kilometre-scale ice-shelf processes.

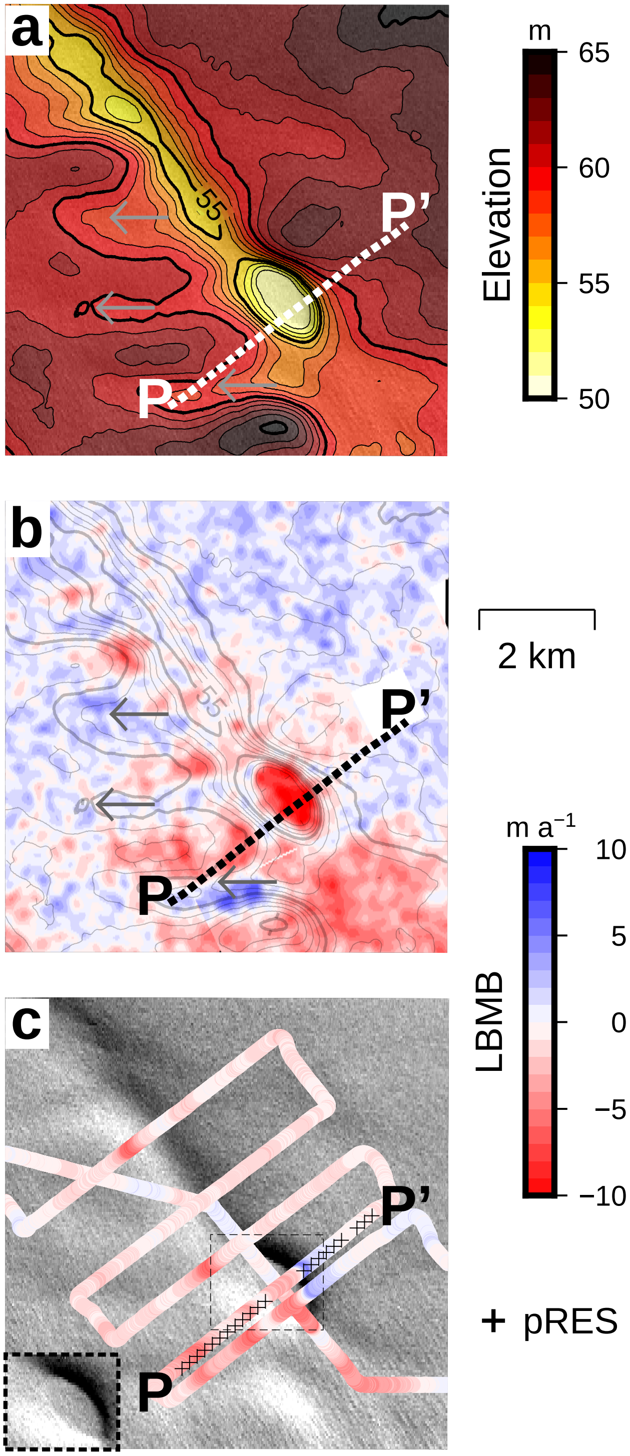

Figure 5. Close-up of the "englacial lake", located as inset c in Fig. 1. (a) Surface elevation from the TanDEM-X DEM of 2014. (b) LBMB (c) Landsat image of 2014 overlaid with the LBMB computed with elevations from the 2014 TanDEM-X DEM and the 2016 GNSS profiles. The crosses locate phase-sensitive radar (pRES) points. The profile PP' is shown in Fig. 6. Subfigures (a) and (b) are overlain with the surface elevation contour lines of 1 m.

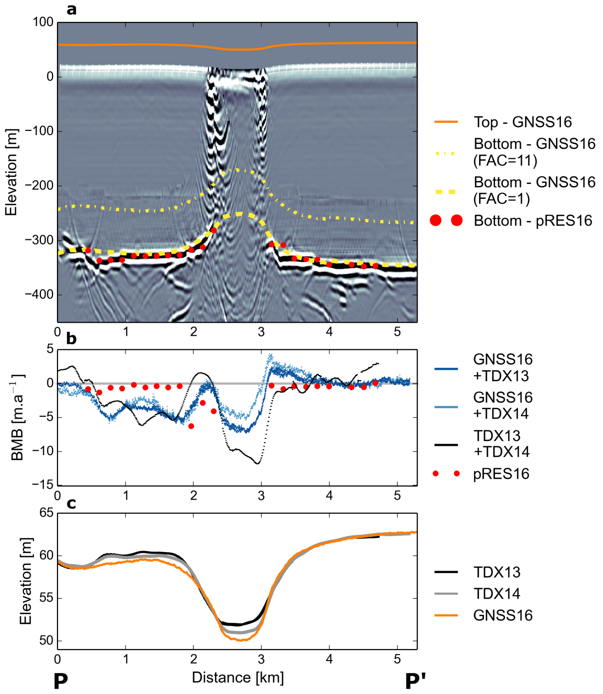

Figure 6. Profile PP' across the ellipsoidal surface depression located in Fig. 5. (a) Radargram and GNSS surface elevation (Top - GNSS16) from 2016 together with the hydrostatic basal elevation (using firn-air content values of 11 and 1) (Bottom - GNSS16) and basal elevation from phase-sensitive radar (pRES). (b) LBMB based on phase-sensitive radar measurement in 2016 (pRES16), TanDEM-X elevation changes between 2013 and 2014 (TDX13+TDX14) and elevation changes between GNSS and TanDEM-X profiles (GNSS16+TDX13, GNSS16+TDX14). (c) Surface lowering at the englacial lake: surface elevation between the GNSS profile of 2016 (GNSS16) and the TanDEM-X profiles from 2013 and 2014 (TDX13 and TDX14). Elevations are referenced to the WGS84 ellipsoid and all profiles are shown in the 2016 geometry.

4 Error sources when deriving the LBMB

4.1 Hydrostatic thickness and Lagrangian thickness change

The Lagrangian thickness change is the dominant error source of the LBMB for the Roi Baudouin Ice Shelf, since both ice-flow divergence and SMB for the Roi Baudouin Ice Shelf are one order of magnitude smaller (Fig. 2). The Lagrangian thinning or thickening depends (i) on the surface elevation and firn density that define the hydrostatic ice thickness, and (ii) on the matching of the DEMs in a Lagrangian framework.

The interferometric DEMs provide excellent spatial resolution at the cost that they require calibration. It is straightforward to offset the DEMs to account for the relative phase unwrapping using Antarctic-wide DEMs based on altimetry. More challenging are residual phase trends that may originate from imprecise satellite orbits/SAR processing (Drews et al., 2009) or represent unaccounted tilting of the ice-shelf surface due to tides. In our case, these trends are near-linear and become evident in the difference fields of neighbouring DEMs. They systematically extend in the azimuth direction with residual height differences typically ranging from -0.5 to +0.5 m. Such biases strongly imprint the corresponding LBMB fields resulting in a mosaic with a linear trend typically ranging from -10 to +10 m a^{-1} in the azimuth direction and cutting edges reaching up to 13 m a^{-1}. To account for this, we applied plane-fitting to the 2014 DEMs (section 2.4). The adjusted DEMs differ from the kinematic GNSS profiles collected in 2016 with -0.2 $\pm$1.1 m in mean and standard deviation, respectively.

Other uncertainties are rooted in referencing the ellipsoidal surface elevation to height above sea level (using the geoid and the mean dynamic topography) which we estimate with $\pm$1 m with little spatial dependency (cf. Drews (2015) for a more detailed discussion on these quantities in the RBIS area).

Along the profile PP', the inferred thickness from radar profiling and from phase-sensitive radar agree closely, but the hydrostatic thickness is >80 m thinner (Fig. 6a). Because surface elevation is well constrained by our kinematic GNSS profiles (Fig. 6c), we attribute this large, unphysical mismatch to an overestimation of the firn-air content. The firn densification model predicts a value of 11 m at that location. However, in the field it became evident that this area is close to a spatially extensive blue-ice area where firn-air content is negligible. Reducing the firn-air content to 1 m reconciles the hydrostatic ice thickness with the observed radar ice thickness (Fig. 6a). Such a large deviation of the modelled firn-air content may be site-specific because it is located in the transition zone where turbulent mixing by the katabatic winds and a wind-albedo feedback form a micro-climate that causes extensive surface melting with not yet fully understood effects on the firn densification (Lenaerts et al., 2017). Moreover, Drews et al. (2016) used wide-angle radar measurements in conjunction with ice coring farther seawards and also found that firn density may vary on small spatial scales, in particular across ice-shelf channels, where surface melt water collects in the corresponding surface depressions and locally refreezes. Therefore, we anticipate that at least some of the variability seen in the LBMB field is due to unresolved variations in firn density. Fortunately, for the Roi Baudouin Ice Shelf this effect is mitigated by the low ice-flow divergence, which renders the absolute value of the hydrostatic ice thickness less important (eq. (1)). This may be different for other ice shelves.

To get our LBMB in a Lagrangian geometry, we matched 5×5 km^2 patches of the two DEMs from 2013 and 2014 using a cross-correlation algorithm (section 2.1). This method works better than matching the DEMs based on flow vectors (as in

Moholdt et al., 2014). This is because the interferometrically-derived velocities used here (Fig. 2c) compare well in magnitude with GNSS measurements (Berger et al., 2016), they are however not sufficiently constrained for the flow direction. Tilts by a few degrees cause misalignment of ice-shelf channels resulting in an erroneous bimodal pattern in the respective LBMB field. The large-scale LBMB patterns, resulting from the two matching techniques, agree well.

4.2 Ice-flow divergence: the benefits of regularized derivatives

The high-resolution velocity field is too noisy in magnitude to approximate the derivatives in the flow divergence with finite differencing of neighbouring cells (gridded to 125 m posting). This can be accounted for by smoothing the velocity field, however, we found that this smears out lateral flow convergence near ice-shelf channels (arrows in Fig. 2d). Because enhanced basal melting beneath ice-shelf channels can cause lateral convergence (Drews, 2015), it is important to preserve this pattern. We found that applying the total-variation regularization (Chartrand, 2011) results in the best trade-off between meaningful derivatives and loss of spatial resolution. Fig. 7 illustrates a close-up of an ice-shelf channel (inset b in Fig. 1) where we compare the velocity divergence and the LBMB based on a smoothed velocity field (averaged within 5.125×5.125 km^2 moving windows) with the velocity divergence and the LBMB calculated using the total-variation regularization (section 2.5). In the regularized case, ice converges more clearly in the channels (velocity divergence up to 3 times lower), which translates in higher basal melt rates (with LBMB 4 m a^{-1}, i.e., ~200%, lower) than in the smoothed case. This effect is localised and subtle on the RBIS (because the Lagrangian thickness change primarily controls the LBMB). Nevertheless, this might not be the case for ice shelves where dynamic thinning is much stronger. This example shows that a high-resolution BMB field does not only depend on high-resolution thickness fields but also on sufficiently fine velocities and de-noised velocity gradients.

4.3 Surface mass balance

Both the firn-air content and the SMB are spatially less well resolved than our ice thickness and velocity fields. Consequently, we do not capture SMB variations associated with ice-shelf channels. Both Drews et al. (2016) and Langley et al. (2014) found evidence in the shallow radar stratigraphy that the SMB may be locally elevated in those areas, potentially reflecting the deposition of drifting snow. Those variations, however, occur over a lateral distance of only a few kilometres and are not resolved by the atmospheric model applied here. The subsequent underestimation of the SMB in the channels therefore results in a positive bias of the LBMB in these areas.

5 Spatial variability of the Lagrangian basal mass balance

The large-scale patches of enhanced basal melting (section 3; labels 1-3 in Fig. 1) are sufficiently far away from the tidal bending zone so that we can safely assume hydrostatic equilibrium. This means that the LBMB likely reflects the true BMB at the ice-shelf base. These regions (especially patches 1 and 2) are also detected by Rignot et al. (2013), based on different input datasets, and line up with the largest gradients in the hydrostatic ice thickness, suggesting that the enhanced basal melting is

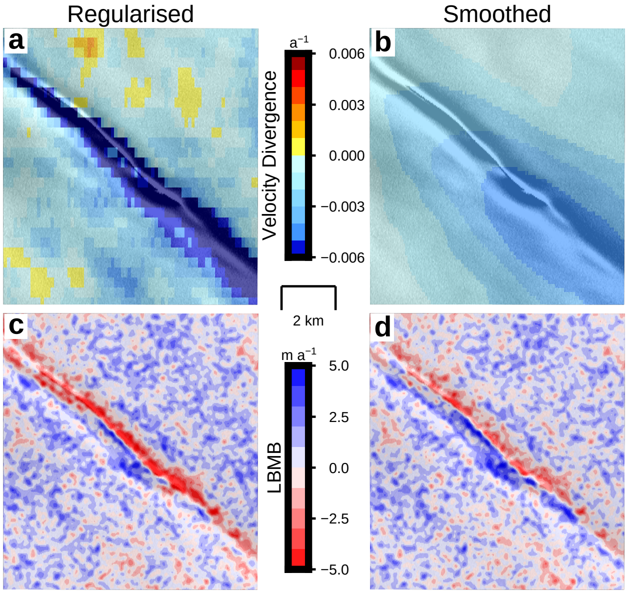

Figure 7. Close-up of inset b in Fig 1. Comparison of regularized (left: a,c) and smoothed (right: b,d) velocity gradients ($\nabla \cdot \boldsymbol{u}$) and their impact resulting velocity divergence (top: a,b) and LBMB (bottom: c,d). The background image is from Landsat 8, acquired in 2014.

driven by the basal ice-shelf slope. Those steeper parts facilitate the slope-dependent entrainment of heat in the mixed layer beneath the ice shelf increasing basal melting (Jenkins and Doake, 1991; Little et al., 2009).

As we have seen, some of the observed variability may reflect unresolved spatial variability in firn density (Drews et al., 2016) or surface lowering that is not hydrostatically compensated. Interpreting the LBMB on sub-kilometre scales is therefore not straightforward. However, the comparison with the phase-sensitive radar data and the kinematic GNSS profiling increases our confidence that much of the relative variability that we observe here is not due to noise. This is most clearly shown for the englacial lake area where the localised surface lowering is consistently observed in different datasets over a 3-year time period. This makes this region dynamically active, although the signal does not necessarily indicate localised basal melting. Two other options are: (i) a transient adjustment of the surface towards hydrostatic equilibrium (Humbert et al., 2015) as a response to some unknown event in the past which locally reduced the ice thickness, and (ii) the surface lowering may reflect vertical creeping of a liquid water body through the ice column. In any case, the surface lowering is restricted to a small area and the ice-shelf channel farther downstream appears passive.

In most areas, ice-shelf channels seem to advect passively and basal melt rates there do not significantly stand out from those in the larger surrounding. We find however some evidence for locally elevated basal melt rates in ice-shelf channels in the ice-shelf's interior (e.g. inset b in Fig. 1, Fig. 7c) and close to the grounding zone (inset a in Fig. 1, Fig.4). Almost all ice-shelf channels at RBIS are connected to the grounding line and may originate from water-filled subglacial conduits injecting basal-melt water into the ice-shelf cavity, driving a spatially localised buoyant melt-water plume (Jenkins, 2011; Le Brocq et al., 2013). Such localised melting near the grounding zone has been previously observed on Pine Island Ice Shelf using similar methods as done here (Dutrieux et al., 2013). However, on Pine Island Ice Shelf, background melt rates are an order of magnitude larger than what is observed here (Depoorter et al., 2013; Rignot et al., 2013) and Dutrieux et al. (2013) analysed DEMs separated by 3 years (compared to the 1 year time period used here). This explains why the BMB gradients appear more clearly in those cases. In areas where the LBMB is elevated beneath ice-shelf channels, we find some evidence that basal melting is concentrated on the flanks, rather than on the apex (Fig. 4). This accords both with observations (Dutrieux et al., 2014) and modelling (Millgate et al., 2013). Inside the channels, those studies show strongest (weakest) melting on the flank (at the apex) of the channels and moderate melting between them. Dutrieux et al. (2014) explain this pattern with the presence of a colder water layer (formed by mixing of melt and sea water (Rignot and Steffen, 2008)) that blocks the heat flux from below near the apex of the channel. Alternatively, modelling (Millgate et al., 2013) suggests that a geostrophic current develops beneath the channels (if the channels are wide enough) which preferentially melts at the channel's flanks.

In summary, our combination of satellite observations with field data shows that much of the sub-kilometric variability that we observe in the LBMB field is above the signal-to-noise ratio. This highlights that ice-ocean interactions vary spatially over the entire ice shelf and implies that point measurements with phase-sensitive radars are not necessarily representative for a larger area. Instead, phase-sensitive radar measurements are best understood in combination with satellite-based estimates covering larger spatial scales. On the other hand, on-site point measurements are crucial to estimate the quality of the satellite-based BMB estimates which are uncertain in their magnitude.

6 Conclusions

We have derived the Lagrangian Basal Mass Balance (LBMB) of the Roi Baudouin Ice Shelf by combining TanDEM-X DEMs of 2013 and 2014 with high-resolution surface velocities and atmospheric modelling. On a large scale, the LBMB shows the highest basal melt rates where the ice draft is steepest, i.e. close to the grounding line and near Derwael Ice Rise and the Western Ice Promontory. This pattern is overlain with significant sub-kilometre scale variability, as witnessed by localised surface lowering of a (potentially refrozen) englacial lake and large basal melting rates below ice-shelf channels. For the latter, we find evidence that at least in some areas, basal melting is concentrated on the channel's flanks as opposed to its apex. Key advancements in our methodology to elucidate this variability are (i) the calibration of the DEMs to account for residual trends from the interferometric processing, (ii) the quality of the matching procedure for calculating the Lagrangian thickness change, and (iii) the total-variation regularization of the spatial derivatives that preserves small-scale flow anomalies near ice-shelf channels. New satellites (such as TanDEM-X or Sentinel 1) will continue to provide highly-resolved datasets of surface elevation and ice velocity. In comparison, atmospheric modelling does not (yet) provide the required spatial resolution on firn-density and SMB to solve the mass budget reliably on sub-kilometre scales. Although the uncertainty of the absolute LBMB values remains high, we find a good fit with on-site measurements from phase-sensitive radar, and we demonstrate that much of the spatial LBMB variability contains information about ice-shelf processes occurring at sub-kilometre scales. This variability highlights the complexity of the ice-ocean and ice-atmosphere interactions on small spatial scales on ice shelves, which need to be accounted for by glaciologists, oceanographers and atmospheric scientists.

Table 1. Input datasets

Type of data	Technique used	Dataset/Model	literature	gridding	Use (Eq.)
Surface elevation	observation	TanDEM-X	this study	10 m	$\frac{\mathrm{D}H}{\mathrm{D}t}$, H
Velocity	observation	ERS1/2 ALOS PALSAR	Berger et al. (2016)	125 m	$\nabla \cdot \boldsymbol{u}$
Surface Mass Balance	modelling	RACMO 2.3	Lenaerts et al. (2017, 2014)	5.5 km	SMB
Firn-air content	modelling	RACMO 2.3	Lenaerts et al. (2017) Ligtenberg et al. (2011)	5.5 km	H
Mean Dynamic topography	modelling	DTU12MDT	Knudsen and Andersen (2012)	0.125°	H
Geoid	modelling	EIGEN-6C4	Förste et al. (2014)	0.125°	H

Appendix A: Input data

Table 1 characterises the main input variable in Eq. (1).

Acknowledgements. This paper forms a contribution to the Belgian Research Programme on the Antarctic (Belgian Federal Science Policy Office), project SD/CA/06A (Constraining Ice Mass Change in Antarctica, IceCon). S. Berger is supported by a FRS-FNRS (Fonds de la Recherche Scientifique) “Aspirant” PhD fellowship. R. Drews was partially supported by the Deutsche Forschungsgemeinschaft (DFG) in the framework of the priority programme “Antarctic Research with comparative investigations in Arctic ice areas” by the grant MA 3347/10-1. S. Sun is supported by the FNRS-PDR (Fonds de la Recherche Scientifique) project MEDRISM. TanDEM-X data originate from German Aerospace Center (ATI-GLAC0267). We thank Nicolas Bergeot (Royal Observatory Belgium) who helped with GNSS processing and K. Nicholls for his valuable help in processing of the phase-sensitive radar. We received excellent logistic support by the Belgian Military, AntarctiQ and the International Polar Foundation during the field campaigns. Finally, we thank J. Lenaerts and S. Ligtenberg for sharing results from atmospheric modelling.

References

Banwell, A. F., MacAyeal, D. R., and Sergienko, O. V.: Breakup of the Larsen B Ice Shelf triggered by chain reaction drainage of supraglacial lakes, Geophysical Research Letters, 40, 5872–5876, doi:10.1002/2013GL057694, http://doi.wiley.com/10.1002/2013GL057694, 2013.

Berger, S., Favier, L., Drews, R., Derwael, J. J., and Pattyn, F.: The control of an uncharted pinning point on the flow of an Antarctic ice shelf, Journal of Glaciology, 62, 37–45, doi:10.1017/jog.2016.7, http://journals.cambridge.org/abstract{_}S0022143016000071, 2016.

Bindschadler, R., Choi, H., Wichlacz, A., Bingham, R., Bohlander, J., Brunt, K., Corr, H., Drews, R., Fricker, H., Hall, M., Hindmarsh, R., Kohler, J., Padman, L., Rack, W., Rotschky, G., Urbini, S., Vornberger, P., and Young, N.: Getting around Antarctica: New high-resolution mappings of the grounded and freely-floating boundaries of the Antarctic ice sheet created for the International Polar Year, The Cryosphere, 5, 569–588, doi:10.5194/tc-5-569-2011, http://www.the-cryosphere.net/5/569/2011/tc-5-569-2011.html, 2011a.

Bindschadler, R., Vaughan, D. G., and Vornberger, P.: Variability of basal melt beneath the Pine Island Glacier ice shelf, West Antarctica, Journal of Glaciology, 57, 581–595, doi:10.3189/002214311797409802, http://www.ingentaconnect.com/content/igsoc/jog/2011/00000057/00000204/art00001, 2011b.

Callens, D., Matsuoka, K., Steinhage, D., Smith, B., Witrant, E., and Pattyn, F.: Transition of flow regime along a marine-terminating outlet glacier in East Antarctica, The Cryosphere, 8, 867–875, doi:10.5194/tc-8-867-2014, http://www.the-cryosphere.net/8/867/2014/tc-8-867-2014.html, 2014.

Callens, D., Drews, R., Witrant, E., Philippe, M., and Pattyn, F.: Temporally stable surface mass balance asymmetry across an Ice rise derived from radar internal reflection horizons through inverse modeling, Journal of Glaciology, 62, 525–534, doi:10.1017/jog.2016.41, http://www.journals.cambridge.org/abstract{_}S0022143016000411, 2016.

Chartrand, R.: Numerical Differentiation of Noisy, Nonsmooth Data, ISRN Applied Mathematics, 2011, 1–11, doi:10.5402/2011/164564, http://downloads.hindawi.com/journals/isrn.applied.mathematics/2011/164564.pdf, 2011.

Chuter, S. J. and Bamber, J. L.: Antarctic ice shelf thickness from CryoSat-2 radar altimetry, Geophysical Research Letters, 42, 10,710–721,729, doi:10.1002/2015GL066515, http://dx.doi.org/10.1002/2015GL066515, 2015.

DeConto, R. M. and Pollard, D.: Contribution of Antarctica to past and future sea-level rise, Nature, 531, 591–597, doi:10.1038/nature17145, http://dx.doi.org/10.1038/nature17145, 2016.

Depoorter, M. A., Bamber, J. L., Griggs, J. a., Lenaerts, J. T. M., Ligtenberg, S. R. M., van den Broeke, M. R., and Moholdt, G.: Calving fluxes and basal melt rates of Antarctic ice shelves., Nature, 502, 89–92, doi:10.1038/nature12567, http://www.ncbi.nlm.nih.gov/pubmed/24037377, 2013.

Drews, R.: Evolution of ice-shelf channels in Antarctic ice shelves, The Cryosphere, 9, 1169–1181, doi:doi:10.5194/tc-9-1169-2015, http://www.the-cryosphere.net/9/1169/2015/tc-9-1169-2015.html, 2015.

Drews, R., Rack, W., Wesche, C., and Helm, V.: A Spatially Adjusted Elevation Model in Dronning Maud Land, Antarctica, Based on Differential SAR Interferometry, IEEE Transactions on Geoscience and Remote Sensing, 47, 2501–2509, doi:10.1109/TGRS.2009.2016081, http://ieeexplore.ieee.org/articleDetails.jsp?arnumber=4895338, 2009.

Drews, R., Matsuoka, K., Martín, C., Callens, D., Bergeot, N., and Pattyn, F.: Evolution of Derwael Ice Rise in Dronning Maud Land, Antarctica, over the last millennia, Journal of Geophysical Research: Earth Surface, 120, 564–579, doi:10.1002/2014JF003246, http://doi.wiley.com/10.1002/2014JF003246, 2015.

Drews, R., Brown, J., Matsuoka, K., Witrant, E., Philippe, M., Hubbard, B., and Pattyn, F.: Constraining variable density of ice shelves using wide-angle radarmeasurements, The Cryosphere, 10, 811–823, doi:10.5194/tc-10-811-2016, http://www.the-cryosphere.net/10/811/2016/, 2016.

Dutrieux, P., Vaughan, D. G., Corr, H. F. J., Jenkins, A., Holland, P. R., Joughin, I., and Fleming, A.: Pine Island Glacier ice shelf melt distributed at kilometre scales, The Cryosphere, 7, 1591–1620, 2013.

Dutrieux, P., Stewart, C., Jenkins, A., Nicholls, K. W., Corr, H. F. J., Rignot, E., and Steffen, K.: Basal terraces on melting ice shelves, Geophysical Research Letters, 41, 5506–5513, 2014.

Favier, L., Gagliardini, O., Durand, G., and Zwinger, T.: A three-dimensional full Stokes model of the grounding line dynamics: effect of a pinning point beneath the ice shelf, The Cryosphere, 6, 101–112, doi:10.5194/tc-6-101-2012, http://www.the-cryosphere.net/6/101/2012/tc-6-101-2012.html, 2012.

Favier, L., Durand, G., Cornford, S. L., Gudmundsson, G. H., Gagliardini, O., Gillet-Chaulet, F., Zwinger, T., Payne, A. J., and Le Brocq, A. M.: Retreat of Pine Island Glacier controlled by marine ice-sheet instability, Nature Climate Change, 4, 117–121, doi:10.1038/nclimate2094, http://dx.doi.org/10.1038/nclimate2094, 2014.

Favier, L., Pattyn, F., Berger, S., and Drews, R.: Dynamic influence of pinning points on marine ice-sheet stability: a numerical study in Dronning Maud Land, East Antarctica, The Cryosphere, 10, 2623–2635, doi:10.5194/tc-10-2623-2016, http://www.the-cryosphere.net/10/2623/2016/, 2016.

Förste, C., Bruinsma, S., Abrikosov, O., Flechtner, F., Marty, J.-C., Lemoine, J.-M., Dahle, C., Neumayer, H., Barthelmes, F., König, R., and Biancale, R.: EIGEN-6C4 - The latest combined global gravity field model including GOCE data up to degree and order 1949 of GFZ Potsdam and GRGS Toulouse, in: EGU General Assembly Conference Abstracts, vol. 16 of *EGU General Assembly Conference Abstracts*, p. 3707, 2014.

Gladish, C. V., Holland, D. M., Holland, P. R., and Price, S. F.: Ice-shelf basal channels in a coupled ice/ocean model, Journal of Glaciology, 58, 1227–1244, doi:10.3189/2012JoG12J003, 2012.

Golledge, N. R., Menviel, L., Carter, L., Fogwill, C. J., England, M. H., Cortese, G., and Levy, R. H.: Antarctic contribution to meltwater pulse 1A from reduced Southern Ocean overturning, Nature Communications, 5, 1–10, doi:10.1038/ncomms6107, http://www.nature.com/doifinder/10.1038/ncomms6107, 2014.

Golledge, N. R., Kowalewski, D. E., Naish, T. R., Levy, R. H., Fogwill, C. J., and Gasson, E. G. W.: The multi-millennial Antarctic commitment to future sea-level rise, Nature, 526, 421–425, doi:10.1038/nature15706, http://www.nature.com/doifinder/10.1038/nature15706, 2015.

Gudmundsson, G. H., Krug, J., Durand, G., Favier, L., and Gagliardini, O.: The stability of grounding lines on retrograde slopes, The Cryosphere, 6, 1497–1505, doi:10.5194/tc-6-1497-2012, http://www.the-cryosphere.net/6/1497/2012/, 2012.

Helm, V., Humbert, A., and Miller, H.: Elevation and elevation change of Greenland and Antarctica derived from CryoSat-2, The Cryosphere, 8, 1539–1559, doi:10.5194/tc-8-1539-2014, http://www.the-cryosphere.net/8/1539/2014/, 2014.

Hulbe, C. L., MacAyeal, D. R., Denton, G. H., Kleman, J., and Lowell, T. V.: Catastrophic ice shelf breakup as the source of Heinrich event icebergs, Paleoceanography, 19, n/a–n/a, doi:10.1029/2003PA000890, http://doi.wiley.com/10.1029/2003PA000890, 2004.

Humbert, A., Steinhage, D., Helm, V., Hoerz, S., Berendt, J., Leipprand, E., Christmann, J., Plate, C., and Müller, R.: On the link between surface and basal structures of the Jelbart Ice Shelf, Antarctica, Journal of Glaciology, 61, 975–986, doi:10.3189/2015JoG15J023, http://www.ingentaconnect.com/content/igsoc/jog/2015/00000061/00000229/art00013, 2015.

Jenkins, A.: Convection-driven melting near the grounding lines of ice shelves and tidewater glaciers, Journal of Physical Oceanography, 41, 2279–2294, 2011.

Jenkins, A. and Doake, C. S. M.: Ice-ocean interaction on Ronne Ice Shelf, Antarctica, Journal of Geophysical Research, 96, 791, doi:10.1029/90JC01952, http://doi.wiley.com/10.1029/90JC01952, 1991.

Jezek, K. and RAMP-Product-Team: RAMP AMM-1 SAR Image Mosaic of Antarctica, Fairbanks, AK: Alaska Satellite Facility, in association with the National Snow and Ice Data Center, Boulder, CO. Digital media, 2002.

Knudsen, P. and Andersen, O. B.: A global mean ocean circulation estimation using goce gravity models - the DTU12MDT mean dynamic topography model, in: 20 Years of Progress in Radar Altimetry Symposium, p. 123, 2012.

Langley, K., Deschwanden, A., Kohler, J., Sinisalo, A., Matsuoka, K., Hattermann, T., Humbert, A., Nøst, O. A., and Isaksson, E.: Complex network of channels beneath an Antarctic ice shelf, Geophysical Research Letters, 41, 1209–1215, 2014.

Le Brocq, A. M., Ross, N., Griggs, J. A., Bingham, R. G., Corr, H. F. J., Ferraccioli, F., Jenkins, A., Jordan, T. A., Payne, A. J., Rippin, D. M., and Others: Evidence from ice shelves for channelized meltwater flow beneath the Antarctic Ice Sheet, Nature Geoscience, 6, 945–948, 2013.

Lenaerts, J., Brown, J., Van Den Broeke, M. R., Matsuoka, K., Drews, R., , Callens, D., Philippe, M., Gorodetskaya, I. V., Van Meijgaard, E., Reijmer, C. H., and Others: High variability of climate and surface mass balance induced by Antarctic ice rises, Journal of Glaciology, 60, 1101, http://www.staff.science.uu.nl/{~}lenae101/pubs/Lenaerts2014c.pdf, 2014.

Lenaerts, J. T. M., Lhermitte, S., Drews, R., Ligtenberg, S. R. M., Berger, S., Helm, V., Smeets, C. J. P. P., van den Broeke, M. R., van de Berg, W. J., van Meijgaard, E., Eijkelboom, M., Eisen, O., and Pattyn, F.: Meltwater produced by wind–albedo interaction stored in an East Antarctic ice shelf, Nature Climate Change, 7, 58–62, doi:10.1038/nclimate3180, http://www.nature.com/doifinder/10.1038/nclimate3180{%}5Cnhttp://www.benemelt.eu/benemelt{#}74887, 2017.

Ligtenberg, S. R. M., Helsen, M. M., and van den Broeke, M. R.: An improved semi-empirical model for the densification of Antarctic firn, The Cryosphere, 5, 809–819, doi:10.5194/tc-5-809-2011, http://www.the-cryosphere.net/5/809/2011/tc-5-809-2011.html, 2011.

Little, C. M., Gnanadesikan, A., and Oppenheimer, M.: How ice shelf morphology controls basal melting, Journal of Geophysical Research, 114, C12 007, doi:10.1029/2008JC005197, http://doi.wiley.com/10.1029/2008JC005197, 2009.

Marsh, O. J., Fricker, H. A., Siegfried, M. R., Christianson, K., Nicholls, K. W., Corr, H. F. J., and Catania, G.: High basal melting forming a channel at the grounding line of Ross Ice Shelf, Antarctica, Geophysical Research Letters, pp. n/a–n/a, doi:10.1002/2015GL066612, http://doi.wiley.com/10.1002/2015GL066612, 2016.

Matsuoka, K., Pattyn, F., Callens, D., and Conway, H.: Radar characterization of the basal interface across the grounding zone of an ice-rise promontory in East Antarctica, Annals of Glaciology, 53, 29–34, doi:10.3189/2012AoG60A106, http://www.ingentaconnect.com/content/igsoc/agl/2012/00000053/00000060/art00004, 2012.

Mercer, J. H.: West Antarctic ice sheet and CO2 greenhouse effect: a threat of disaster, Nature, 271, 321–325, doi:10.1038/271321a0, http://www.nature.com/doifinder/10.1038/271321a0, 1978.

Millgate, T., Holland, P. R., Jenkins, A., and Johnson, H. L.: The effect of basal channels on oceanic ice-shelf melting, Journal of Geophysical Research: Oceans, 118, 6951–6964, doi:10.1002/2013JC009402, http://dx.doi.org/10.1002/2013JC009402, 2013.

Moholdt, G., Padman, L., and Fricker, H. A.: Basal mass budget of Ross and Filchner-Ronne ice shelves, Antarctica, derived from Lagrangian analysis of ICESat altimetry, Journal of Geophysical Research: Earth Surface, 2014.

Neckel, N., Drews, R., Rack, W., and Steinhage, D.: Basal melting at the Ekström Ice Shelf, Antarctica, estimated from mass flux divergence, Annals of Glaciology, 53, 294–302, doi:10.3189/2012AoG60A167, http://www.ingentaconnect.com/content/igsoc/agl/2012/00000053/00000060/art00035, 2012.

Nicholls, K. W., Corr, H. F., Stewart, C. L., Lok, L. B., Brennan, P. V., and Vaughan, D. G.: A ground-based radar for measuring vertical strain rates and time-varying basal melt rates in ice sheets and shelves, Journal of Glaciology, 61, 1079–1087, doi:10.3189/2015JoG15J073, http://www.ingentaconnect.com/content/igsoc/jog/2015/00000061/00000230/art00005, 2015.

Padman, L., Fricker, H. A., Coleman, R., Howard, S., and Erofeeva, L.: A new tide model for the Antarctic ice shelves and seas, Annals of Glaciology, 34, 247–254, 2002.

Padman, L., Erofeeva, S. Y., and Fricker, H. A.: Improving Antarctic tide models by assimilation of ICESat laser altimetry over ice shelves, Geophysical Research Letters, 35, L22 504, doi:10.1029/2008GL035592, http://doi.wiley.com/10.1029/2008GL035592, 2008.

Paolo, F. S., Fricker, H. A., and Padman, L.: Volume loss from Antarctic ice shelves is accelerating., Science, 348, 327–331, doi:10.1126/science.aaa0940, http://www.sciencemag.org/content/early/2015/03/31/science.aaa0940.abstract, 2015.

Pattyn, F., Perichon, L., Durand, G., Favier, L., Gagliardini, O., Hindmarsh, R. C., Zwinger, T., Albrecht, T., Cornford, S., Docquier, D., Fürst, J. J., Goldberg, D., Gudmundsson, G. H., Humbert, A., Hütten, M., Huybrechts, P., Jouvet, G., Kleiner, T., Larour, E., Martin, D., Morlighem, M., Payne, A. J., Pollard, D., Rückamp, M., Rybak, O., Seroussi, H., Thoma, M., and Wilkens, N.: Grounding-line migration in plan-view marine ice-sheet models: results of the ice2sea MISMIP3d intercomparison, Journal of Glaciology, 59, 410–422, doi:10.3189/2013JoG12J129, http://www.ingentaconnect.com/content/igsoc/jog/2013/00000059/00000215/art00002, 2013.

Rignot, E. and Steffen, K.: Channelized bottom melting and stability of floating ice shelves, Geophysical Research Letters, 35, 2008.

Rignot, E., Mouginot, J., and Scheuchl, B.: Ice flow of the Antarctic ice sheet, Science, 333, 1427–1430, doi:10.1126/science.1208336, 2011.

Rignot, E., Jacobs, S., Mouginot, J., and Scheuchl, B.: Ice-shelf melting around Antarctica, Science, 341, 266–270, doi:10.1126/science.1235798, 2013.

Rignot, E., Mouginot, J., Morlighem, M., Seroussi, H., and Scheuchl, B.: Widespread, rapid grounding line retreat of Pine Island, Thwaites, Smith, and Kohler glaciers, West Antarctica, from 1992 to 2011, Geophysical Research Letters, 2014.

Ritz, C., Edwards, T. L., Durand, G., Payne, A. J., Peyaud, V., and Hindmarsh, R. C. A.: Potential sea-level rise from Antarctic ice-sheet instability constrained by observations, Nature, 528, 115–118, doi:10.1038/nature16147, http://dx.doi.org/10.1038/nature16147, 2015.

Scambos, T. A., Bohlander, J. A., Shuman, C. A., and Skvarca, P.: Glacier acceleration and thinning after ice shelf collapse in the Larsen B embayment, Antarctica, Geophysical Research Letters, 31, L18 402, doi:10.1029/2004GL020670, 2004.

Schoof, C.: Ice sheet grounding line dynamics: Steady states, stability, and hysteresis, Journal of Geophysical Research, 112, F03S28, doi:10.1029/2006JF000664, http://doi.wiley.com/10.1029/2006JF000664, 2007.

Shean, D. E., Christianson, K., Larson, K. M., Ligtenberg, S. R., Joughin, I. R., Smith, B. E., and Stevens, C. M.: In situ GPS records of surface mass balance and ocean-induced basal melt for Pine Island Glacier, Antarctica, The Cryosphere Discussions, pp. 1–30, doi:10.5194/tc-2016-288, http://www.the-cryosphere-discuss.net/tc-2016-288/, 2017.

Stanton, T. P., Shaw, W. J., Truffer, M., Corr, H. F. J., Peters, L. E., Riverman, K. L., Bindschadler, R., Holland, D. M., and Anandakrishnan, S.: Channelized ice melting in the ocean boundary layer beneath Pine Island Glacier, Antarctica, Science, 341, 1236–1239, doi:10.1126/science.1239373, http://www.ncbi.nlm.nih.gov/pubmed/24031016, 2013.

Tsai, V. C., Stewart, A. L., and Thompson, A. F.: Marine ice-sheet profiles and stability under Coulomb basal conditions, Journal of Glaciology, 61, 205–215, doi:10.3189/2015JoG14J221, http://www.ingentaconnect.com/content/igsoc/jog/2015/00000061/00000226/art00001, 2015.

Vaughan, D. G., Corr, H. F. J., Bindschadler, R. A., Dutrieux, P., Gudmundsson, G. H., Jenkins, A., Newman, T., Vornberger, P., and Wingham, D. J.: Subglacial melt channels and fracture in the floating part of Pine Island Glacier, Antarctica, Journal of Geophysical Research, 117, doi:10.1029/2012jf002360, http://dx.doi.org/10.1029/2012JF002360, 2012.

Wouters, B., Martin-Español, a., Helm, V., Flament, T., van Wessem, J. M., Ligtenberg, S. R. M., van den Broeke, M. R., and Bamber, J. L.: Dynamic thinning of glaciers on the Southern Antarctic Peninsula, Science, 348, 899–903, doi:10.1126/science.aaa5727, http://www.sciencemag.org/content/348/6237/899.abstract, 2015.